A universal kinetic equation solver for radiation belts

Liheng Zheng[1], Lunjin Chen[1], Anthony A. Chan[2], Peng Wang[3], Zhiyang Xia[1], and Xu Liu[1]

[1]William B. Hanson Center for Space Sciences, Department of Physics, University of Texas at Dallas, Richardson, Texas, USA.

[2]Department of Physics and Astronomy, Rice University, Houston, Texas, USA.

[3]Department of Earth, Planetary and Space Sciences, University of California at Los Angeles, Los Angeles, California, USA.

Key Points:

- A numerical solver is developed for the general form of kinetic equations that appear in radiation belt study.
- The solver works in arbitrarily given coordinate systems up to 3D, with freedom in specifying boundary geometry and boundary conditions.
- Based on the SDE method, the solver's numerical efficiency is greatly improved by a variance reduction technique.

Corresponding author: Liheng Zheng, `zhengliheng@gmail.com`

Abstract

Recent proceedings in the radiation belt studies have proposed new requirements for numerical methods to solve the kinetic equations involved. In this article, we present a numerical solver that can solve the general form of radiation belt Fokker-Planck equation and Boltzmann equation in arbitrarily provided coordinate systems, and with user-specified boundary geometry and boundary conditions. The solver is based upon the mathematical theory of stochastic differential equations, whose computational accuracy and efficiency are greatly enhanced by specially designed adaptive algorithms and variance reduction technique. The versatility and robustness of the solver is exhibited in three example problems. The solver applies to a wide spectrum of radiation belt modeling problems, including the ones featuring nonlinear wave-particle interactions.

1 Introduction

A widely adopted method to study the dynamics of radiation belts is to solve a kinetic equation describing the evolution of particle phase space density. In quasi-linear theory, this kinetic equation is usually a Fokker-Planck equation that takes the general covariant form (Schulz, 1991)

$$\frac{\partial f}{\partial t} = \frac{1}{G}\frac{\partial}{\partial Q^\mu}\left(GD^{\mu\nu}\frac{\partial f}{\partial Q^\nu}\right) - \frac{1}{G}\frac{\partial}{\partial Q^\mu}\left(Gh^\mu f\right) + Sf + v, \tag{1}$$

where f is the phase-averaged phase space density, $G = \det(\frac{\partial J^\mu}{\partial Q^\nu})$ is the Jacobian determinant for the transformation from canonical action variables J^μ ($\mu = 1, 2, 3$) to the generalized coordinates Q^μ, and $D^{\mu\nu}$, h^μ, S and v are coefficients of the equation. Summation on repeated Greek indices is implied throughout this paper. In different radiation belts, the number of terms emerging on the right-hand side of Eq. (1) and their respective physical backgrounds may be different. For the Earth's outer radiation belt, the second and the fourth terms are usually missing; the first term represents diffusion caused by wave-particle interactions, and the third term is often a loss characterized by the particle lifetime (e.g., W. Li & Hudson, 2019, and the reference therein). In the low-altitude inner radiation belt where wave-particle interactions are not as significant, the first and the second terms are often provided by the diffusion and dynamic friction caused by interparticle Coulomb collisions (e.g., Selesnick, 2012), and the fourth term may be a source from cosmic ray albedo neutron decay (CRAND) (e.g., Selesnick, 2015; X. Li et al., 2017). For radiation belts of the gas giants, all terms could be present (e.g., Horne et al., 2008; Lorenzato et al., 2012). The first two terms may be attributable to both wave-particle

48   interactions and inter-particle collisions, and in addition, synchrotron radiation, which

49   is negligible in Earth's radiation belts, bleeds energy for the ultra-relativistic electrons

50   and thus also contributes to the second term (e.g., Bolton et al., 2002, 2004). The third

51   term could represent the moon-sweeping loss, and the fourth term may come from moon

52   volcanic activities as a plasma source (e.g., Nénon et al., 2017).

53   The left-hand side of Eq. (1) describes the dynamical trajectory of a phase space

54   volume element according to Liouville's theorem (e.g., Goldstein, 1980, Chap. 9), and

55   the absence of spatial derivatives there is due to the vanishing Poisson bracket $[f, H]$ for

56   the phase-averaged f and the phase-independent particle Hamiltonian H. In some cir-

57   cumstances, it is more desirable to discern the dependence of f on certain phases ϕ^ι (but

58   which remains averaged over other phases), then after expanding the Poisson bracket,

59   Eq. (1) becomes

$$\frac{\partial f}{\partial t} + \dot{\phi}^\iota \frac{\partial f}{\partial \phi^\iota} = \frac{1}{G}\frac{\partial}{\partial Q^\mu}\left(GD^{\mu\nu}\frac{\partial f}{\partial Q^\nu}\right) - \frac{1}{G}\frac{\partial}{\partial Q^\mu}\left(Gh^\mu f\right) + Sf + v, \qquad (2)$$

61   where a dot over ϕ^ι indicates its time derivative, and the equation is now a Boltzmann

62   equation in the context of radiation belts. The most common situation is perhaps the

63   dependence of f on the drift phase, which in the Earth's outer radiation belt may be caused

64   by the wave activity dependence on magnetic local time (e.g., Shprits et al., 2009), and

65   in the inner belt by the longitudinal variation of drift shell altitude (e.g., Tu et al., 2010;

66   Xiang et al., 2019).

67   Various numerical models have been built to solve a specific form of either Eq. (1)

68   or Eq. (2) (e.g., Beutier et al., 1995; Selesnick et al., 2003; Tao et al., 2008; Albert et al.,

69   2009; Subbotin et al., 2010; Tu et al., 2013; Zheng et al., 2014; Wang et al., 2017; Xi-

70   ang et al., 2020, to name a few), and each of them is built with a hard-coded choice of

71   coordinates and roughly fixed number of equation terms; therefore, each model is only

72   applicable to a specific set of problems. Yet for some compelling problems there is not

73   a numerical model known to the authors; for example, a drift-phase resolved inner ra-

74   diation belt model with fully incorporated diffusion, advection and source terms may be

75   the key to understanding the effects of lightning-generated and man-made very-low-frequency

76   waves to the electron precipitation (e.g., Rodger et al., 2003; Sauvaud et al., 2008), or

77   to assessing the relative significance of Earthward diffusion versus CRAND as the pos-

78   sible electron source (e.g., Cunningham et al., 2018; Xiang et al., 2020). It is the pur-

79   pose of this article to present a numerical code, named UBER (for "universal Boltzmann

80 equation solver"), that solves Eq. (1) and Eq. (2) in an arbitrarily user-specified coor-

81 dinate system up to three dimensions, with great freedom in specifying boundary geom-

82 etry and boundary conditions, and with various combinations of equation terms. There-

83 fore, it is expected that the solver can be applied to a wide spectrum of radiation belt

84 modeling problems. More importantly, it has the potential to asymptotically solve the

85 nonlinear wave-particle interaction kinetic equation formulated in Artemyev et al. (2018),

86 and thereby provides a viable means to incorporate nonlinear effects into global radia-

87 tion belt modeling.

88 The underlying mathematical theory of the solver is stochastic differential equa-

89 tion (SDE) theory. The SDE method had been utilized by Tao et al. (2008), Selesnick

90 et al. (2013) and Zheng et al. (2014) in their modeling of the radiation belts. The method

91 is grid-free, and enjoys unparalleled advantages in dealing with cross diffusion compo-

92 nents and complicated boundary geometry (e.g., Zheng et al., 2016), but is meanwhile

93 notorious for low efficiency ascribed to its Monte Carlo nature. In this article, we also

94 describe specially designed numerical techniques that have enhanced the computational

95 speed of the SDE method by an order of magnitude, thus making the solver much af-

96 fordable to large-scale simulations. Three example problems with distinct physical back-

97 grounds are provided in this article to demonstrate the abilities and versatility of the solver.

2 Mathematical Theory

99 The kinetic equations (1) and (2) are parabolic partial differential equations (PDEs).

100 Written in the Kolmogorov backward form (see below), a parabolic PDE corresponds to

101 a multi-dimensional SDE that describes the motion of an Itô stochastic process whose

102 functional expectation obeys the PDE; and the PDE can then be solved by calculating

103 path integrals of the corresponding stochastic process (e.g., Freidlin, 1985; Øksendal, 1998).

104 Let us consider the following partial differential problem composed of a Kolmogorov

105 backward equation and a set of initial and boundary conditions:

$$\partial_t f = \frac{1}{2} a^{\mu\nu}(t, \boldsymbol{x}) \partial_\mu \partial_\nu f + b^\mu(t, \boldsymbol{x}) \partial_\mu f + c(t, \boldsymbol{x}) f + u(t, \boldsymbol{x}), \tag{3}$$

$$f(0, \boldsymbol{x}) = g_0(\boldsymbol{x}), \quad \boldsymbol{x} \in \bar{\Omega}, \tag{4}$$

$$f(t, \boldsymbol{x}) = g_1(t, \boldsymbol{x}), \quad \boldsymbol{x} \in \partial_1 \Omega, \tag{5}$$

$$\hat{\boldsymbol{\gamma}}(\boldsymbol{x}) \cdot \nabla f - \lambda(t, \boldsymbol{x}) f = 0, \quad \boldsymbol{x} \in \partial\Omega \setminus \partial_1 \Omega, \tag{6}$$

110   where ∂_t and ∂_μ are shorthands for the partial differentials with respect to t and the μ-

111   th coordinate, respectively. In Eqs. (4)-(6), $\bar{\Omega}$ denotes the closure of the domain and $\partial\Omega$

112   its boundary. In particular, $\partial_1\Omega$ are the boundary pieces of the first type (Dirichlet) bound-

113   ary condition, and $\partial\Omega\backslash\partial_1\Omega$ indicate the boundary pieces excluding those in $\partial_1\Omega$, which

114   are of the second (Neumann, $\lambda \equiv 0$) or the third type (Robin, $\lambda \neq 0$) boundary con-

115   ditions. The unit vector $\hat{\gamma}$ points into $\bar{\Omega}$ and is not tangent to the local boundary.

116   The mathematical theory of SDEs establishes a relation between Eqs. (3)-(6) and

117   the Itô stochastic process, whose spatial positions are denoted by the random variable

118     $\boldsymbol{X}_s$ in Ω, that obeys the reflected SDE

$$dX_s = \boldsymbol{b}(t - s, \boldsymbol{X}_s)ds + \boldsymbol{\sigma}(t - s, \boldsymbol{X}_s) \cdot d\boldsymbol{W}_s + \hat{\boldsymbol{\gamma}}(\boldsymbol{X}_s)dk_s, \tag{7}$$

120   where the dot product on the right-hand side is between a rank-2 tensor and a vector,

121   and the parameter s runs from 0 to t, so that the stochastic process retrogrades in time

122   from t to 0. The first term on the right-hand side describes the ballistic part of its mo-

123   tion. The second term describes the stochastic part, with the coefficient tensor $\boldsymbol{\sigma}$ sat-

124   isfying $\boldsymbol{\sigma}\cdot\boldsymbol{\sigma}^T = \mathbf{a}$ (whose components are $a^{\mu\nu}$). Note that this condition does not uniquely

125   determine $\boldsymbol{\sigma}$, but all satisfying $\boldsymbol{\sigma}$'s are equivalent (Levi's theorem, Freidlin, 1985; Zheng

126   et al., 2014). $\boldsymbol{W}_s$ is a vector Wiener process of the same dimensions as $\boldsymbol{X}_s$, with each

127   dimension an independent Gaussian stochastic variable that has zero mean and variance

128   s. The third term describes reflection of the stochastic process in the direction given by

129     $\hat{\gamma}$ on the boundary $\partial\Omega\backslash\partial_1\Omega$, and k_s is a monotonic stochastic variable that only increases

130   when the stochastic process is on that boundary to force $\boldsymbol{X}_s$ to stay in $\bar{\Omega}$. k_s can thus

131   be considered as a measure of the time that the stochastic process spent on $\partial\Omega\backslash\partial_1\Omega$,

132   and hence has the name local time. The Itô process stops either in $\bar{\Omega}$ when $s = t$, or

133   on $\partial_1\Omega$ at $s = \tau < t$.

134   A formal solution of the problem in Eqs. (3)-(6) is given by the Feynman-Kac for-

135   mula (e.g., Kac, 1949; Øksendal, 1998; Klebaner, 2005)

$$f(t, \boldsymbol{x}) = \mathbb{E}\big[\mathcal{F}^{t,\boldsymbol{x}}[\boldsymbol{X}_s]\big], \tag{8}$$

137   in which $\mathbb{E}$ is the expectation operator, and $\mathcal{F}^{t,\boldsymbol{x}}[\boldsymbol{X}_s]$ is a functional of the stochastic path

138      $\boldsymbol{X}_s$ started from t and $\boldsymbol{x}$, and has the expression

139
$$\mathcal{F}^{t,\boldsymbol{x}}[\boldsymbol{X}_s] = \mathbb{I}_{\tau \geq t}\, g_0(\boldsymbol{X}_t) \exp\left[\int_0^t c(t-s, \boldsymbol{X}_s)ds - \int_0^t \lambda(t-s, \boldsymbol{X}_s)dk_s \right]$$

140
$$+ \mathbb{I}_{\tau < t}\, g_1(t-\tau, \boldsymbol{X}_\tau) \exp\left[\int_0^\tau c(t-s, \boldsymbol{X}_s)ds - \int_0^\tau \lambda(t-s, \boldsymbol{X}_s)dk_s \right]$$

141
$$+ \int_0^{t\wedge\tau} u(t-s, \boldsymbol{X}_s) \exp\left[\int_0^s c(t-r, \boldsymbol{X}_r)dr - \int_0^s \lambda(t-r, \boldsymbol{X}_r)dk_r \right]ds, \quad (9)$$

142   where the symbol $\mathbb{I}_{\tau \geq t}$ is equal to one when $\tau \geq t$, which means the stochastic process

143   has stopped in $\bar{\Omega}$ before it had a chance to reach $\partial_1 \Omega$, and zero otherwise; and $t \wedge \tau$ means

144   the smaller between the two. Physically, the functional $\mathcal{F}^{t,\boldsymbol{x}}[\boldsymbol{X}_s]$ is a propagator of con-

145   tribution carried along the stochastic path from either the initial condition or the first

146   type boundary condition to the point of solution, and the exponential functions indicate

147   how this contribution enhances or decays along this path.

148   To formally solve the Fokker-Planck equation (1) by the Feynman-Kac formula (8),

149   it remains to transform the equation together with its proper initial and boundary con-

150   ditions into the form of Eqs. (3)-(6). To this end, directly expanding Eq. (1) and collect-

151   ing terms with the same differentiation order yields its Kolmogorov backward form

152
$$\partial_t f = D^{\mu\nu}\partial_\mu\partial_\nu f + \left[(\partial_\nu D^{\mu\nu} + D^{\mu\nu}\partial_\nu \ln G) - h^\mu\right]\partial_\mu f + \left[S - (\partial_\mu h^\mu + h^\mu \partial_\mu \ln G)\right]f + v. \quad (10)$$

153   Comparing Eq. (10) with Eq. (3), we thus have the correspondences of coefficients that:

154
$$\begin{cases} \boldsymbol{a} = 2\mathbf{D}, \\ \boldsymbol{b} = \nabla \cdot \mathbf{D} - \boldsymbol{h}, \\ c = S - \nabla \cdot \boldsymbol{h}, \\ u = v, \end{cases} \quad (11)$$

155   where in curvilinear coordinates, the divergence operator on a tensor field $\boldsymbol{\Gamma}$ is

156
$$\nabla \cdot \boldsymbol{\Gamma} = \partial_\mu \Gamma^{\mu\cdots} + \Gamma^{\mu\cdots}\partial_\mu \ln G, \quad (12)$$

157   in which the dots stand for all other indices irrelevant to the operation, and the terms

158      $\partial_\mu \ln G$ come from summation of the Christoffel symbols in a covariant derivative (e.g.,

159   Mathews & Walker, 1970, Chap. 15). It is worth remarking that $-\boldsymbol{h}$ appears in the ex-

160   pression for $\boldsymbol{b}$, so that the Itô process travels against the advection velocity. This is in-

161   deed the case since it is time-backwards. Also, from the expression for c, divergence of

162   the advection serves as a loss of phase space density.

163   Initial and boundary conditions to Eq. (1) are transformed as follows. For the ini-

164   tial condition and the first type boundary condition, values of $f(t, \boldsymbol{x})$ are specified just

165   as in Eqs. (4) and (5). For a flux boundary condition of the form $\Phi = g_2(t, \boldsymbol{x})f$, we note

166   that the outward flux Φ across a boundary is given by $(\hat{\boldsymbol{n}} \cdot \mathbf{D} \cdot \nabla f - \hat{\boldsymbol{n}} \cdot \boldsymbol{h} f)$, with $\hat{\boldsymbol{n}}$ the

167   unit inward normal vector of $\partial\Omega \backslash \partial_1\Omega$. Therefore, the corresponding boundary condi-

168   tion is

169
$$\hat{\boldsymbol{n}} \cdot \mathbf{D} \cdot \nabla f - (\hat{\boldsymbol{n}} \cdot \boldsymbol{h} + g_2)f = 0. \tag{13}$$

170   Comparing Eq. (13) with Eq. (6), we identify that:

171
$$\begin{cases} \hat{\boldsymbol{\gamma}} = \dfrac{\hat{\boldsymbol{n}} \cdot \mathbf{D}}{|\hat{\boldsymbol{n}} \cdot \mathbf{D}|}, \\ \lambda = \dfrac{\hat{\boldsymbol{n}} \cdot \boldsymbol{h} + g_2}{|\hat{\boldsymbol{n}} \cdot \mathbf{D}|}. \end{cases} \tag{14}$$

172   Although the SDE (7) does not prevent $\boldsymbol{\sigma}$, and hence $\mathbf{D}$, from being zero, the expres-

173   sions in Eqs. (14) do become singular for vanishing $\mathbf{D}$ on $\partial\Omega \backslash \partial_1\Omega$. In the region where

174   $\mathbf{D}$ vanishes, Eq. (3) is no longer parabolic but degenerates to an advection equation (a

175   first order PDE), for which imposing a Neumann or Robin boundary condition is over-

176   determinant. In this case, we invoke on the boundary minimal diffusion in the eigen-direction

177   of $\hat{\boldsymbol{n}}$ so that $\hat{\boldsymbol{\gamma}} = \hat{\boldsymbol{n}}$, and let $g_2 \equiv -\hat{\boldsymbol{n}} \cdot \boldsymbol{h}$ so that $\lambda = 0$, which means the advective

178   flow is free to cross the boundary. The situation that $\mathbf{D}$ is finite but $|\hat{\boldsymbol{n}} \cdot \mathbf{D}|$ vanishes is

179   considered pathological to our problem.

180   Up to this point, we have transformed the Fokker-Planck equation (1) and its ini-

181   tial and boundary conditions to the problem in Eqs. (3)-(6), and gathered all expressions

182   in Eqs. (11) and (14) for the constructing components of the SDE (7) as well as the func-

183   tional (9). In order to solve the Boltzmann equation (2), it suffices for us to just trans-

184   form the equation into the form of Eq. (1). To this end, we enlarge the phase space by

185   concatenating the coordinates Q^μ and ϕ^ι, so that $x^\xi = \{Q^\mu, \phi^\iota\}$, and introduce the new

186   coefficients $\widetilde{D}^{\xi\eta}$, $\widetilde{h}^\xi$, $\widetilde{S}$ and $\widetilde{v}$ that satisfy the following conditions:

187
$$\begin{cases} \widetilde{D}^{\mu\nu} = D^{\mu\nu}, \quad \widetilde{D}^{\xi\iota} = 0, \\ \widetilde{h}^\xi = \{h^\mu, \dot{\phi}^\iota\}, \\ \widetilde{S} = S + \partial_\iota \dot{\phi}^\iota, \\ \widetilde{v} = v. \end{cases} \tag{15}$$

188   It can be verified that Eq. (1) in the x^ξ coordinates with the new coefficients given by

189   (15) transforms into Eq. (2) after replacing x^ξ by Q^μ and ϕ^ι. The transformation (15)

190   essentially treats ϕ^ι as new dimensions of the stochastic motion, except that the stochas-

Table 1. User input items to the UBER code

Input items	Comments
$\partial_\mu \ln G$	Vector field to specify the coordinate system
$D^{\mu\nu}$, h^μ, S, v	Coefficients to define the PDE
$g_0(x^\mu)$	Function to provide the initial condition
$\psi(t, x^\mu) = 0$	Equation to define a boundary piece's geometry
$g_*(t, x^\mu)$	Function to provide the boundary condition,
	$* = 1$ or 2 depending on the type of the boundary
$\hat{\boldsymbol{n}}(x^\mu)$	Inward unit normal vector only for $\partial\Omega \setminus \partial_1\Omega$

A set of the boundary-related items for each piece of boundary.

tic part of the motion in these dimensions is identically zero. A new type of boundary condition might emerge for problems involving Eq. (2), that is the periodic boundary condition for the phases ϕ^ι. From the viewpoint of stochastic motion, though, such periodicity is not really a boundary but rather a topology of Ω. The treatment of periodic boundary condition will be exemplified in the third problem in Section 4 below.

To summarize this section, the above mathematical theory allows us to fully define a PDE problem involving Eq. (1) or Eq. (2) in an arbitrary coordinate system given the input functions and equations as listed in Table 1, which can be either analytical or numerical in the UBER code. The equation terms may be freely turned off by setting their corresponding coefficients zero. The number of boundary pieces is totally up to choice, which can even be zero to put the boundary at infinity. The boundary geometry may be time-variable for boundary pieces in $\partial_1\Omega$, but must be fixed for those in $\partial\Omega \setminus \partial_1\Omega$. Solutions of this problem are obtained once we find a way to evaluate the functional in Eq. (9) for a realization of a stochastic path, and to estimate the expectation of the functional. These numerical techniques are the subject of the next section.

3 Numerical Techniques

We give an outline of the algorithms used by the UBER code in this section, with emphasis on the techniques that improve both its accuracy and efficiency. Lower-level numerical techniques, such as the generation of pseudo-random variables, linear algebraic

210 operations, and parallelized computation, are based on the works presented in Zheng (2015).

211 The general idea for numerically implementing the SDE method is as follows: (i) for a

212 given spatiotemporal position $(t, \boldsymbol{x})$ where an equation solution is wanted, a number of

213 stochastic paths starting from this common position are simulated; (ii) for each stochas-

214 tic path, its functional value is evaluated by the path integrals as in Eq. (9); and (iii) from

215 these sampled functional values, their expectation is estimated, and this gives the solu-

216 tion at $(t, \boldsymbol{x})$. Therefore, the SDE method is essentially a Monte Carlo method. It does

217 not rely on a computational grid, and is able to solve the problem locally. However, in

218 many occasions it is still worth obtaining global solutions on a grid, so that the solutions

219 at time stamp T_i may be used as the initial condition for the solutions at T_{i+1}, analo-

220 gous to the idea of the layer methods (e.g., Tao et al., 2009). In this way, the stochas-

221 tic processes need only to be simulated for a short duration of $t = T_{i+1} - T_i$ to obtain

222 the new solutions, for which the calculation of functional expectation would converge much

223 faster than those simulated for the full length $t = T_{i+1}$. The only operation on this grid

224 would be interpolation and possibly extrapolation, therefore unlike in the layer meth-

225 ods, the grid needs not to be uniform or even regular.

226 Integration of the SDE (7) employs the Euler-Maruyama scheme that is order 1

227 for weak convergence problems such as ours, meaning that when only the statistical dis-

228 tribution of stochastic paths matters but not the individual path, the expectation of the

229 schematic error is proportional to the first power of the time stepsize (Kloeden & Platen,

230 1992). To further reduce the schematic error, an adaptive time stepsize is used in UBER.

231 It can be shown that (e.g., Zheng, 2015) the root-mean-square (RMS) distance an Itô

232 stochastic process travels in infinitesimal time ds is

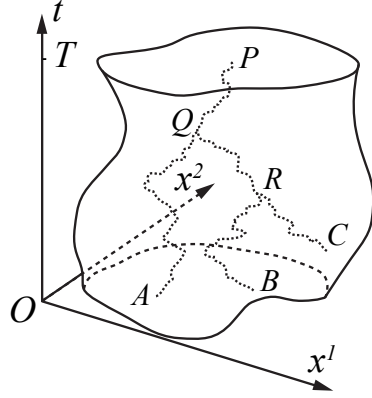$$d\bar{X}_s = \sqrt{\mathrm{tr}(\mathbf{a})ds}. \tag{16}$$

234 Numerically, the first order contribution from $\boldsymbol{b}\Delta s$ cannot be neglected due to the finite

235 Δs. Therefore, we prescribe a desired RMS spatial stepsize $\Delta\bar{X}_s$, which is sufficiently

236 small compared to the size of Ω and any scale length of the equation coefficients, and

237 then choose the smaller Δs inferred from either Eq. (16) or $\Delta\bar{X}_s = \boldsymbol{b}\Delta s$ at every step

238 of integration as the adaptive stepsize. This scheme evidently reduces to a simple adap-

239 tive Euler scheme for integrating ordinary differential equations when $\mathbf{a}$ approaches zero.

240 Oblique reflection of the stochastic process on $\partial\Omega\backslash\partial_1\Omega$ and the calculation of dk_s

241 follow the projected-half-space algorithm presented in Gobet (2001), which is also or-

der 1 in the weak convergence sense. The idea is that, for an exact half-space boundary, k_s can be proven to share the same probabilistic distribution with a composite stochastic variable involving $\boldsymbol{W}_s$, coefficients of the SDE, the normal vector $\hat{\boldsymbol{n}}$, and an independent exponential random variable with parameter $(2s)^{-1}$ (Lépingle, 1995), and therefore k_s can be explicitly calculated by these known quantities. For general smooth boundary geometry, an additional contribution to dk_s may also come from possible projection along the $\hat{\boldsymbol{\gamma}}$ direction needed to keep the stochastic process within domain. With dk_s obtained and the SDE (7) integrated, the functional (9) can be readily evaluated by an ordinary numerical integration technique implemented along the realized stochastic path.

Expectation of the functionals can be estimated, in principle, from an arithmetic mean of a number N of sampled stochastic path integrals. The error of this estimation, $\epsilon = |\mathbb{E}[\mathcal{F}^{t,\boldsymbol{x}}] - \langle \widetilde{\mathcal{F}}^{t,\boldsymbol{x}} \rangle|$ where a tilde is used to indicate a numerical realization in this section and $\langle \cdots \rangle$ indicates averaging over samples, can be estimated by dividing the simulation of stochastic processes into batches (Zheng, 2015). Although the probabilistic distribution of individual $\widetilde{\mathcal{F}}^{t,\boldsymbol{x}}$ is generally far from normal and largely unknown, that for the batch-wise mean of $\widetilde{\mathcal{F}}^{t,\boldsymbol{x}}$ approaches a Gaussian for a large enough sample number per batch due to the central limit theorem, and thereby a confidence interval can be calculated for the batch-wise means using the Student t-distribution (e.g., Kloeden & Platen, 1992). We use this confidence interval as an approximation to ϵ. In this way, UBER adaptively stops simulating more batches of stochastic processes when the estimated error meets a prescribed tolerance.

In typical radiation belt problems, the functional values from various stochastic paths may differ by orders of magnitude, hence their contributions to the arithmetic mean also differ by orders of magnitude, whereas their computational efforts are of the same order. Therefore, straightforward calculation of their arithmetic mean could result in extremely slow convergence with N and squander computational power. To reduce statistical variance in this procedure, a process-splitting technique is developed based on the idea of importance sampling, i.e., to make "denser" sampling in more important "regions". In conventional Monte Carlo methods, the "region" is an "area" in a parameter space, and importance sampling effectively splits one sample point therein that would have made a huge contribution to the calculation into many sample points nearby, while weights of these samples are reduced accordingly to keep the probabilistic distribution of samples unbiased (e.g., Press et al., 1992). But unlike conventional Monte Carlo methods, the

Figure 1. Schematic illustration of process splittings in a $t \otimes \mathbb{R}^2$ space. A stochastic process travels backward in time from point P and splits into two at point Q, where its projected functional value is found to be sufficiently large (see text for exact meaning). One child process splits again at point R where its projected functional value is found to be even larger. The independent child processes would eventually stop either in $\bar{\Omega}$ as at points A and B, or on $\partial_1\Omega$ as at point C.

samples in the SDE method are paths which belong to a functional space. To still implement this idea, we split the stochastic path when it is projected to contribute a large functional value.

Fig. 1 gives an illustration of this technique in a $t \otimes \mathbb{R}^2$ space. As a stochastic path being integrated from point P, the functional value of the entire path (from $s = 0$ to $s = t$) is continuously predicted based on the partial path that has been realized. This projected functional value is compared to the value of some quantile (e.g., the 80th percentile) statistically derived from all previously completed stochastic paths starting from the same position. When at some place Q, the projected functional value falls above this quantile, the stochastic process is deemed to make a significant contribution to the arithmetic mean. It is then split into a number of child processes at Q, and each child process traces down an independent path thereafter. These child paths, together with their common parent path segment PQ, hence constitute "nearby samples" in the functional space. This procedure can be further iterated if the projected functional value later falls into an even higher quantile (e.g., the 90th percentile), as shown at R. After all procedures finished, the eventual result is a tree structure of stochastic paths rooted at P. For

291   the illustration in Fig. 1, the actual functional value of the path PQA will be weighted

292   by 1/2, and those of $PQRB$ and $PQRC$ will be weighted by 1/4, when calculating their

293   contributions to the mean. In the UBER code, a practical choice for the number of chil-

294   dren at each splitting is 4, and that for the upper limit of offspring generations is 3, so

295   that a stochastic process can be split into a maximum of $4^3 = 64$ processes. Effects of

296   the process-splitting technique are studied in the first problem in the next section.

297   It still remains to find a method to project the functional value of a stochastic path

298   when it is only partially realized. For this purpose, we insert a break point at $s = s' \in$

299     $(0, t)$ to the integrations in Eq. (9) and see how it transforms. We simplify the situation

300   by only considering the stochastic processes stopping in $\bar{\Omega}$ for the moment, and denote

301   the following functional integrals:

$$\mathcal{U}_0^t = \exp\left(\int_0^t c\,ds - \int_0^t \lambda\,dk_s\right), \tag{17}$$

$$\mathcal{V}_0^t = \int_0^t u \exp\left(\int_0^s c\,dr - \int_0^s \lambda\,dk_r\right) ds, \tag{18}$$

304   in which the integrand functions c, λ and u are as those in Eq. (9). Then, the functional

305     $\mathcal{F}^{t,\boldsymbol{x}}$ with the above presumptions and notations is transformed as

$$
\begin{aligned}
\mathcal{F}^{t,\boldsymbol{x}} &= g_0(\boldsymbol{X}_t)\mathcal{U}_0^t + \mathcal{V}_0^t \\
&= g_0(\boldsymbol{X}_t)\mathcal{U}_0^{s'}\mathcal{U}_{s'}^t + \left(\mathcal{V}_0^{s'} + \mathcal{U}_0^{s'}\mathcal{V}_{s'}^t\right) \\
&= \left[g_0(\boldsymbol{X}_t)\mathcal{U}_{s'}^t + \mathcal{V}_{s'}^t\right]\mathcal{U}_0^{s'} + \mathcal{V}_0^{s'} \\
&= \mathcal{F}^{t-s',\boldsymbol{X}_{s'}}\mathcal{U}_0^{s'} + \mathcal{V}_0^{s'}, \tag{19}
\end{aligned}
$$

310   where $\mathcal{F}^{t-s',\boldsymbol{X}_{s'}}$ is the functional for a stochastic process that starts from the break point

311     $(t - s', \boldsymbol{X}_{s'})$ and continues till $s = t$.

312   Suppose that a partial path has been realized up to $s = s'$, from it we can read-

313   ily evaluate $\mathcal{U}_0^{s'}$ and $\mathcal{V}_0^{s'}$ in Eq. (19), and therefore need an estimated $\bar{\mathcal{F}}^{t-s',\boldsymbol{X}_{s'}}$ to project

314   the functional value $\bar{\mathcal{F}}^{t,\boldsymbol{x}}$, where a bar is put over all unrealized entities. Specifically, we

315   would need these three estimates: $\bar{\boldsymbol{X}}_t$, $\bar{\mathcal{U}}_{s'}^t$ and $\bar{\mathcal{V}}_{s'}^t$. In principle, a good estimation of $\bar{\boldsymbol{X}}_t$

316   is given by integrating along the streamline of the $\boldsymbol{b}(t-s, \boldsymbol{x})$ field through $\boldsymbol{X}_{s'}$ till $s =$

317   t, that is, projecting for $\bar{\boldsymbol{X}}_t$ along the ballistic trajectory of motion while ignoring all the

318   stochasticity since the Wiener process has zero mean. However, this integration is not

319   much cheaper than the realization of $\mathcal{F}^{t-s',\boldsymbol{X}_{s'}}$ itself, and thus is unaffordable. In an-

320   ticipation that the total time length t would not be too large, especially when using a

solution grid, and that $\boldsymbol{b}(t-s, \boldsymbol{x})$ would not vary drastically in this time interval, mapping $\bar{\boldsymbol{X}}_t$ along the constant vector $\boldsymbol{b}(t-s', \boldsymbol{X}_{s'})$ is a good enough but much cheaper approximation. If $\bar{\boldsymbol{X}}_t$ is mapped out of $\bar{\Omega}$ so that $g_0(\bar{\boldsymbol{X}}_t)$ is unable to be evaluated, the particular stochastic process is then disabled from splitting.

The functional values $\bar{\mathcal{U}}_{s'}^t$ and $\bar{\mathcal{V}}_{s'}^t$ are estimated by assuming that, for all possible stochastic paths belonging to the same solution point, there exist mean functions $\bar{c}$, $\bar{\lambda}$ and $\bar{u}$ that are independent of time, and that the mean local time is proportional to the total time length of the stochastic process, so that $\bar{k}_s = \bar{k}s$ with $\bar{k}$ the proportionality constant. Under these assumptions, $\bar{\mathcal{U}}_{s'}^t$ and $\bar{\mathcal{V}}_{s'}^t$ can be expressed by

$$
\begin{aligned}
\bar{\mathcal{U}}_{s'}^t &= \exp\left(\bar{c}\int_{s'}^t ds - \bar{\lambda}\int_{s'}^t dk_s\right) \\
&= \exp\left[(\bar{c}t - \bar{\lambda}\bar{k}t) - (\bar{c}s' - \bar{\lambda}\bar{k}s')\right] \\
&= \frac{\bar{\mathcal{U}}_0^t}{\exp\left(\dfrac{s'}{t}\ln\bar{\mathcal{U}}_0^t\right)},
\end{aligned}
\tag{20}
$$

and

$$
\bar{\mathcal{V}}_{s'}^t = \frac{\bar{\mathcal{V}}_0^t}{\bar{\mathcal{U}}_0^t - 1}\left[\bar{\mathcal{U}}_0^t - \exp\left(\frac{s'}{t}\ln\bar{\mathcal{U}}_0^t\right)\right],
\tag{21}
$$

if $\bar{\mathcal{U}}_0^t \neq 1$, or by

$$
\bar{\mathcal{U}}_{s'}^t = 1,
\tag{22}
$$

$$
\bar{\mathcal{V}}_{s'}^t = \bar{\mathcal{V}}_0^t\left(1 - \frac{s'}{t}\right),
\tag{23}
$$

if $\bar{\mathcal{U}}_0^t = 1$. The values of $\bar{\mathcal{U}}_0^t$ and $\bar{\mathcal{V}}_0^t$ can be well estimated respectively by the medians of $\widetilde{\mathcal{U}}_0^t$ and $\widetilde{\mathcal{V}}_0^t$ that are obtained from all previously completed stochastic paths. Medians are preferred to means here because the probabilistic distributions of these functionals are usually very skewed and heavy-tailed. This projection mechanism would become statistically more accurate as more stochastic processes having been simulated.

4 Example Problems

Three example problems are provided in this section. In the first problem, we solve a Fokker-Planck equation with two source terms, one proportional to the unknown function and the other independent of the unknown function, in both spherical coordinate system and Cartesian coordinate system. Effects of the process-splitting technique are analyzed in this example. In the second problem, an advection-dominated Fokker-Planck equation is considered. We further show that, even for a pure advection equation, the

350   UBER code still gives the correct solutions, although it is not designed for such an equa-

351   tion and may not be the most efficient method. In the last problem, we simulate the Earth's

352   inner radiation belt by solving its Boltzmann equation involving realistic pitch-angle dif-

353   fusion and CRAND source. The treatment of periodic boundary conditions is illustrated

354   in this example.

355   ### 4.1 Problem 1: Neutron Generation and Diffusion in Nuclear Material

356   In this problem, we consider the diffusion and generation of neutrons in a spher-

357   ical nuclear material at detonation, with an initially injected Gaussian neutron distri-

358   bution from a small source at the center, and a neutron-reflecting coat that allows only

359   one half of the surface neutrons to escape. In a spherical coordinate system, the equa-

360   tion, initial condition and boundary conditions are (Serber, 1992)

361
$$\frac{\partial f}{\partial t} = \frac{1}{r^2}\frac{\partial}{\partial r}\left(r^2 D\frac{\partial f}{\partial r}\right) + Sf + v(r), \tag{24}$$
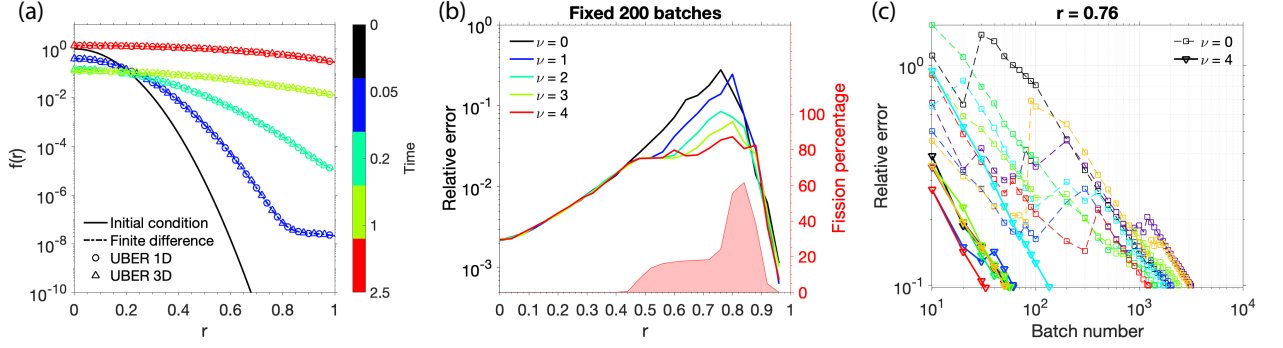
362
$$f(0,r) = \exp\left(-\frac{r^2}{0.02}\right), \tag{25}$$

363
$$\left.\frac{\partial f}{\partial r}\right|_{r=0} = 0, \tag{26}$$

364
$$\left.\left(D\frac{\partial f}{\partial r} + \frac{1}{2}f\right)\right|_{r=1} = 0, \tag{27}$$

365   where f is neutron density, the constant diffusion coefficient $D = 0.1$, the constant rate

366   of neutron generation from chain reaction $S = 2.5$, and $v(r) = 10^{-6}/(1+r)$ character-

367   izes a weak source of neutrons spontaneously emitted in the material. The values and

368   functional forms of these coefficients are solely designed for demonstration purpose and

369   are not meant to be experimentally accurate.

370   UBER solutions are obtained at four time stamps, and are compared with those

371   from a staggered-grid finite difference method (e.g., Ames, 2014), as shown in Fig. 2a.

372   A turning point is observed in the solutions at $T = 0.05$, which marks the transition

373   of neutron source from that dominated by the chain reaction at high background den-

374   sity to that dominated by the spontaneous emission at low density. As time goes by, ef-

375   fect of the spontaneous emission is overwhelmed by the fast-growing chain reaction. Even

376   though the solutions span 8 orders of magnitude, the UBER results are virtually iden-

377   tical to the finite difference ones, and statistical fluctuation which is a typical feature in

378   Monte Carlo methods is not observed in these solutions due to the adaptive algorithms

379   and the variance reduction technique.

Figure 2. (a) UBER and finite difference solutions (dashed line) to the problem in Eqs. (24)-(27). The UBER 1D solutions (circles) are obtained in a one-dimensional spherical coordinate system, and the UBER 3D solutions (triangles) are obtained in three-dimensional Cartesian coordinates along a sphere radius. (b) Left y-axis: The relative errors of the UBER 3D solutions at $T = 0.05$, respectively obtained with the same total number of stochastic processes (2048 per batch) but different upper limits of offspring generations (ν) in the process-splitting technique. $\nu = 0$ means the process-splitting is turned off. Right y-axis: The percentage of stochastic processes undergone splitting for $\nu = 4$. (c) The reduction of relative errors with increasing number of stochastic processes at the slowest converging solution point ($r = 0.76$), for $\nu = 0$ (dashed line and squares) and 4 (solid line and triangles). Colors denote different numerical experiments.

To demonstrate UBER's ability in multiple dimensions with a complicated boundary geometry, the same problem is also solved in a three-dimensional Cartesian coordinate system along a sphere radius. In this coordinate system, the diffusion coefficient becomes a rank-3 tensor with each diagonal component equal to D, and the boundary condition in Eq. (27) is applied to the only boundary that is a sphere with unit radius. The solutions are over-plotted in Fig. 2a. Consistence between the one-dimensional and the three-dimensional results is quite evident.

To analyze the effects of the process-splitting technique, we repeated the three-dimensional solutions at $T = 0.05$, but with a fixed number of stochastic processes (2048 samples per batch, 200 batches) for each solution point and with various upper limits of the off-

390 spring generations ν. $\nu = 0$ indicates that process-splitting technique is disabled. For

391 a fixed number of samples, the relative error of a solution is proportional to the square-

392 root of the variance of sampled functional values, and determines how fast the calcula-

393 tion of expectation converges. The relative errors as functions of r are plotted against

394 the left y-axis of Fig. 2b, and each curve is in fact formed by the medians from eight in-

395 dependent and identical numerical experiments to be more statistically representative.

396 In the range $0.4 < r < 0.9$, the relative errors are consistently reduced with higher

397 offspring generations. At the slowest converging point $r = 0.76$, the process-splitting

398 technique with a maximum of 4 offspring generations could reduce the relative error by

399 an order of magnitude compared to that without splitting. For this curve ($\nu = 4$), the

400 percentages of stochastic processes undergone splitting are plotted as shaded area against

401 the right y-axis. For $r < 0.4$, the relative errors are small and computational conver-

402 gence is fast enough, process-splitting is automatically suppressed by the code to achieve

403 an optimal speed. When the relative errors would have been large, usually a small frac-

404 tion of split stochastic processes could be rather effective.

405 To further reveal the behavior of the process-splitting technique, Fig. 2c plots how

406 the relative error reduces with increasing number of samples (N) in the Monte Carlo pro-

407 cedure for the solution point at $r = 0.76$. There are eight independent and identical

408 numerical experiments respectively for $\nu = 0$ and 4, and each line represents the results

409 from one numerical experiment. The general trend is that the relative error reduces lin-

410 early in a log-log scale plot, resembling its dependence on $N^{-1/2}$. However, without process-

411 splitting, the relative error often jumps up sharply due to the occurrence of a very low

412 probability sample that made a very large contribution, which severely slows down the

413 computational convergence. With process-splitting, such jumps are largely avoided; and

414 on average, the code uses just a little more than 1/100 of the samples without process-

415 splitting to achieve the same relative error of 0.1.

416 In practical UBER usage, solutions are achieved with a prescribed tolerance of rel-

417 ative error and an adaptive number of samples. Therefore, the fast convergence with process-

418 splitting technique could save a significant amount of computational effort even with its

419 extra computational burden. Table 2 lists the normalized wall clock time consumed by

420 UBER for obtaining the solution curve in three dimensions at $T = 0.05$ with a relative

421 error tolerance of 0.1 and a range of maximum offspring generations in process-splitting.

422 Again, each of these numbers is the median from eight independent and identical numer-

Table 2. Normalized wall clock time versus maximum offspring generations (ν) for the UBER 3D solutions at $T = 0.05$

ν	Normalized wall clock time*
0	1
1	0.40
2	0.18
3	0.13
4	0.13

* Median value from eight independent numerical tests.

ical experiments. With $\nu = 3$ and 4, the code is nearly an order of magnitude faster than that without process-splitting. The same wall clock time in these two cases indicates that the faster convergence with more offspring generations starts to be traded off by the computational overhead associated with more complicated splitting, and therefore further increasing ν would not be optimal.

4.2 Problem 2: Magnetized Plasma Evolution Under Instability

In the second problem, we consider a Fokker-Planck equation for the pitch-angle distribution of a magnetized plasma (e.g., Dendy, 1990). Suppose that the electrons are initially in a $\sin^2(x)$ background pitch-angle distribution where x is the pitch angle. An electron beam is injected into the system centered at pitch angle $x = 0.4$. In addition to pitch-angle diffusion, the injected beam excites some kind of plasma instability that kinetically transports the distribution toward $\pi/2$ pitch angle. The equation, initial condition and boundary conditions are written as:
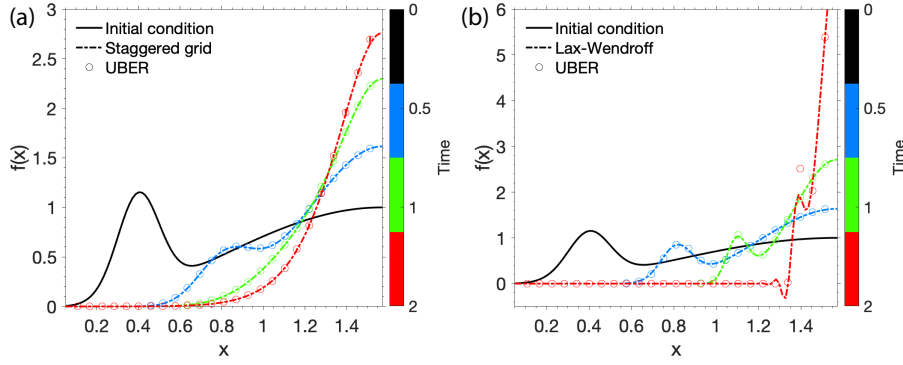
$$\frac{\partial f}{\partial t} = \frac{1}{G}\frac{\partial}{\partial x}\left[GD(t,x)\frac{\partial f}{\partial x}\right] - \frac{1}{G}\frac{\partial}{\partial x}\left[Gh(x)f\right], \tag{28}$$

$$f(0,x) = \sin^2(x) + \exp\left[-\frac{(x-0.4)^2}{0.02}\right], \tag{29}$$

$$f|_{x=0.05} = 0, \tag{30}$$

$$\left.\frac{\partial f}{\partial x}\right|_{x=\pi/2} = 0, \tag{31}$$

where f is the electron distribution function, the Jacobian determinant $G = \sin(x)$, the diffusion coefficient $D(t,x) = (1/2\pi^2)\,\mathrm{erf}(t/2)[1 + \sin^2(2x)]$, and the advection coeffi-

Figure 3. (a) UBER (circles) and staggered-grid finite difference (dashed line) solutions to the problem in Eqs. (28)-(31). (b) UBER (circles) and Lax-Wendroff (dashed line) solutions to the same problem but with zero diffusion.

cient $h(x) = \cos(x)$. Note that, in most of the x range, the advection coefficient is about an order of magnitude larger than the diffusion coefficient. Eq. (30) indicates a loss cone at pitch angle $x = 0.05$. UBER solutions for this problem are plotted in Fig. 3a as circles, and are in excellent agreement with those from the staggered-grid finite difference method. In these solutions, the beam evolves toward $x = \pi/2$ because of the kinetic advection. As the system relaxes, the beam eventually merges into the background, and a final stable distribution is then approached.

Eq. (28) degenerates to a continuity equation if pitch-angle diffusion is turned off by setting $D(t, x)$ to zero. Even for such a pure advection problem, UBER can still obtain accurate and robust solutions as compared to the widely used Lax-Wendroff method (e.g., Ames, 2014), as shown in Fig. 3b. Before $T = 2$, an advection of the beam toward $x = \pi/2$ is seen in the solutions without dispersion, and UBER results are almost identical to the Lax-Wendroff ones. The system, however, is unstable due to the positive advection velocity at $x < \pi/2$ and the zero advection velocity at $x = \pi/2$, so that the electron distribution will be piled up near $x = \pi/2$ and ultimately evolve into a singularity. For this reason, the Lax-Wendroff method begins to fail at $T = 2$ by generating unphysical negative solutions near $x = 1.3$, and will be divergent henceforth. UBER nonetheless gives the correct results that still resolve the peak height and position of the beam.

4.3 Problem 3: Earth's Inner Radiation Belt Simulation

In the last problem, we demonstrate UBER's ability to solve a radiation belt Boltz-mann equation by performing an inner radiation belt simulation involving both the stably trapped (out of the drift loss cone) and the quasi-trapped (in the drift loss cone) electron populations. Inspired by Xiang et al. (2020), we consider the 304-keV electrons at McIlwain's $L_M = 1.25$, which are subject to pitch-angle scattering caused by Coulomb collisions with upper atmospheric neutrals and ionospheric ions and electrons. The equation, initial condition and boundary conditions are:

$$\frac{\partial f}{\partial t} + \omega_d \frac{\partial f}{\partial \phi} = \frac{1}{G} \frac{\partial}{\partial \alpha_0} \left(G D_{\alpha\alpha} \frac{\partial f}{\partial \alpha_0} \right) + \frac{S_e}{p^2}, \tag{32}$$

$$f(0, \phi, \alpha_0) = 0, \tag{33}$$

$$f|_{\phi=0} = f|_{\phi=2\pi}, \tag{34}$$

$$f|_{\alpha_0=\alpha_L} = 0, \tag{35}$$

$$\left. \frac{\partial f}{\partial \alpha_0} \right|_{\alpha_0=\pi/2} = 0. \tag{36}$$

In Eq. (32),

$$\omega_d = \frac{3cLR_E}{e\mu_E} \frac{p^2}{m_e} \frac{D(\sin\alpha_0)}{T(\sin\alpha_0)} \tag{37}$$

is the drift frequency evaluated using dipole-field approximation (Schulz, 1991), in which c is the speed of light in vacuum, L is dipole L-shell, R_E is the radius of Earth, e is the elementary charge, μ_E is the magnetic moment of Earth's intrinsic dipole field, m_e is electron mass, p is electron momentum, α_0 is electron equatorial pitch angle, and the functions $D(\sin\alpha_0)$ and $T(\sin\alpha_0)$ are bounce motion integrals in dipole field that are given in Schulz (1991, pp. 205-210). For simplicity, we ignore the dependence of ω_d on drift phase ϕ, so that the drift phase becomes equivalent to geomagnetic longitude. The Jacobian determinant $G = T(\sin\alpha_0)\sin(2\alpha_0)$. The bounce-averaged pitch-angle diffusion rate is empirically given by

$$D_{\alpha\alpha} = 10^{-5} \exp\left\{ 92.55 \left[\cos^4\alpha_0 - \cos^4\alpha_L(\phi) \right] \right\} + 10^{-9} \quad (\text{s}^{-1}), \tag{38}$$

which features quantitative resemblance with that calculated by realistic atmosphere and ionosphere models in Xiang et al. (2020). In this expression, $\alpha_L(\phi)$ is the bounce loss cone angle dependent on geomagnetic longitude that is determined by drift-shell tracing in the International Geomagnetic Reference Field (IGRF, Finlay et al., 2010). $D_{\alpha\alpha}$ as a function of ϕ and α_0 is plotted in Fig. 4a: it is only significant near the bounce loss
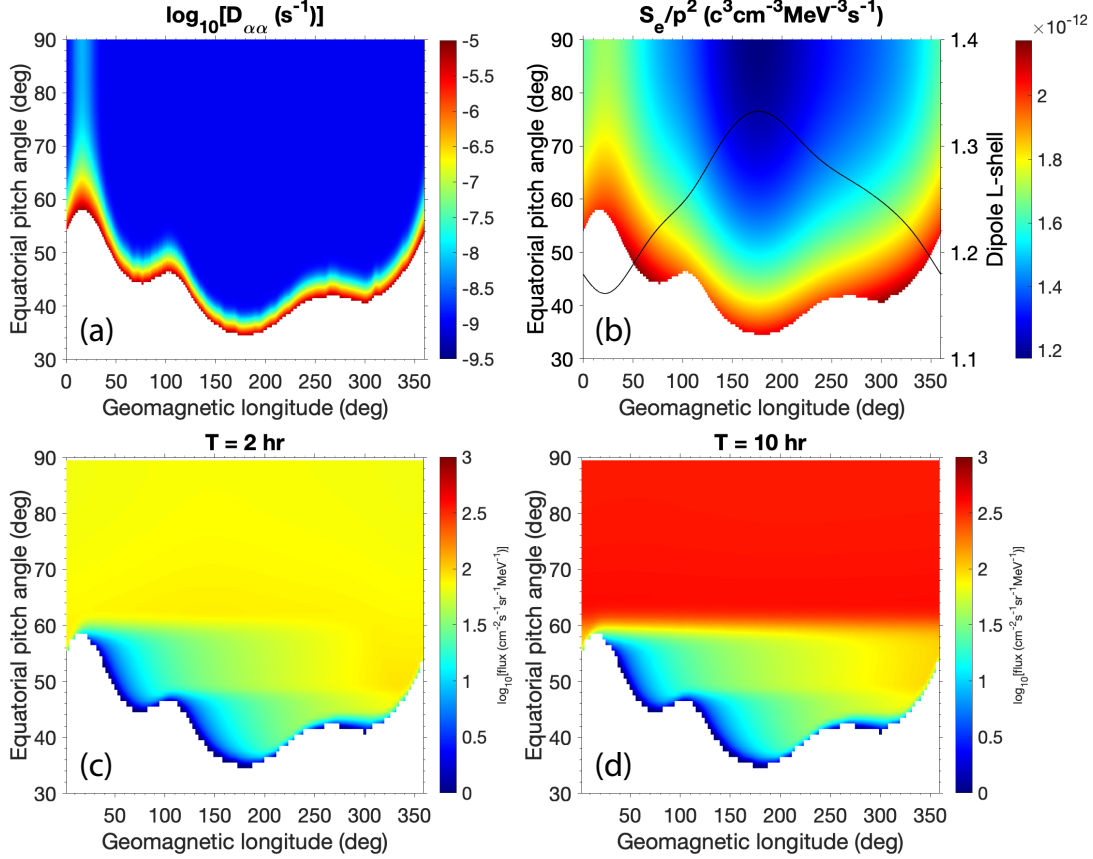
cone and in the South Atlantic Anomaly (SAA) centered at about 20° geomagnetic longitude, due to the closer proximity of the drift shell to the upper atmosphere in these regions. The CRAND source rate S_e/p^2 is approximated by (Lenchek et al., 1961; Selesnick, 2015)

$$\frac{S_e}{p^2} \approx 1.7 \times 10^{-12} \frac{(E_{max} - E)^2}{L^{2.7} \sin \alpha_0} \quad (\text{c}^3\text{cm}^{-3}\text{MeV}^{-3}\text{s}^{-1}), \tag{39}$$

where E_{max} is the maximum kinetic energy (782 keV) available to electrons from neutron β-decay and E is the electron kinetic energy in question, both are measured in unit of the electron rest energy (511 keV), and L is the dipole L-shell, which is a variable dependent on geomagnetic longitude due to multipoles of the Earth's magnetic field. Fig. 4b plots the CRAND source rate as well as the dipole L-shell values corresponding to McIlwain's $L_M = 1.25$ obtained from drift-shell tracing in IGRF, which vary from less than 1.2 in the SAA to above 1.3 near 180° geomagnetic longitude.

Eq. (34) specifies the periodic boundary condition for the drift phase ϕ. In the UBER code, the periodic boundary condition is not really considered a boundary condition; rather, it is dealt with by extending the computational domain to include multiple periods, so that the Itô stochastic processes would not move out of the domain within the given time duration, except for stopping on other first type boundaries. For this specific problem, the time stamp for obtaining solutions is every 2 hours, and the 304-keV electrons drift eastwards with drift periods a little longer than 2 hours. Therefore, the computational domain is extended for one extra period of ϕ from -2π to 0 since the stochastic processes retrograde in time. However, solutions are only sought in the right half of the domain for ϕ between 0 and 2π at each time stamp, and after that, they are copied to the left half to form the entire initial condition for the next time stamp.

The simulation is performed with an initially empty radiation belt as indicated by Eq. (33), and electrons are gradually generated by the CRAND source and meanwhile lost to the bounce loss cone. Fig. 4c and 4d show the solution electron fluxes calculated from $j = fp^2$ after 2 hours and 10 hours, respectively. The characteristic west-east electron flux gradient is formed for the quasi-trapped population ($\alpha_0 < 60°$) within the first 2 hours, and does not change much over time because the SAA sweeps these electrons out every drift period. Weak pitch-angle diffusion of electron fluxes from the quasi-trapped population toward the stably trapped population can be observed at $T = 2$ hours, when the stably trapped fluxes are still low; at $T = 10$ hours, direction of the pitch-angle dif-

Figure 4. (a) Bounce-averaged pitch-angle diffusion coefficient $D_{\alpha\alpha}$ (s^{-1}) for 304-keV electrons. Blank area is in the bounce loss cone. (b) CRAND electron source rate S_e/p^2 (c^{3}cm^{-3}MeV^{-3}s^{-1}) for 304-keV electrons. Black line plots the variation of dipole L-shell versus geomagnetic longitude against the right y-axis, corresponding to the McIlwain's $L_M = 1.25$. (c) Calculated electron fluxes (cm^{-2}s^{-1}sr^{-1}MeV^{-1}) at $T = 2$ hours. (d) Calculated electron fluxes (cm^{-2}s^{-1}sr^{-1}MeV^{-1}) at $T = 10$ hours.

fusion is reversed. Even with atmospheric loss, the CRAND source is strong enough to continuously contribute to the trapped electron fluxes, which are increased by one order of magnitude in 8 hours. These results are quantitatively comparable to those of Xiang et al. (2020).

5 Conclusion and Discussion

In conclusion, we have built a numerical solver for the general form of kinetic equations that appear in radiation belt studies. Based on the SDE method, the solver is coded to work in arbitrarily provided coordinate systems up to three dimensions, with user-

531 specified boundary geometry, boundary conditions, and equation terms. We have also

532 designed adaptive algorithms and a variance reduction technique for the SDE method,

533 which had enhanced its computational speed by one order of magnitude in our test. The

534 example problems in this article demonstrated the solver's versatility and robustness in

535 dealing with a range of problems that might each require a different solver in other meth-

536 ods. The solver, named UBER, has been programmed into a FORTRAN library that

537 can be easily incorporated with other more complicated space physics models.

538 Several other forms of radiation belt kinetic equation should also be solvable by the

539 method presented in this article. In formulating the Boltzmann equation (2), we have

540 assumed that the particle Hamiltonian H is independent of phases of particle motion.

541 For lower-energy ring current particles, the convective electric field potential energy is

542 not negligible in their Hamiltonian, and therefore H would be dependent on the drift phase.

543 As such, expanding the Poisson bracket $[f, H]$ on the left-hand side of the Boltzmann

544 equation will result in additional terms involving partial differentials with respect to the

545 generalized momenta Q^μ. For a radiation belt model including ring current particles, the

546 general form of Boltzmann equation will be

$$\frac{\partial f}{\partial t} + \dot{\phi}^\iota \frac{\partial f}{\partial \phi^\iota} + \dot{Q}^\mu \frac{\partial f}{\partial Q^\mu} = \dots, \tag{40}$$

548 in which the omitted right-hand side of the equation is exactly the same as that of Eq. (2).

549 The Boltzmann equations of the so-called four-dimensional radiation belt models, such

550 as the CIMI model (Fok et al., 2014), the VERB-4D model (Aseev et al., 2016), and the

551 K2 MHD-particle model (Elkington et al., 2019) are of this type. Similar to the treat-

552 ment of Eq. (2), Eq. (40) can be transformed into the form of Eq. (1) by concatenating

553 the coordinates into $x^\xi = \{Q^\mu, \phi^\iota\}$, and performing the following transformation of equa-

554 tion coefficients:

$$\begin{cases} \widetilde{D}^{\mu\nu} = D^{\mu\nu}, \quad \widetilde{D}^{\xi\iota} = 0, \\ \widetilde{h}^\xi = \{h^\mu + \dot{Q}^\mu, \dot{\phi}^\iota\}, \\ \widetilde{S} = S + \partial_\xi \dot{x}^\xi + \dot{Q}^\mu \partial_\mu \ln G, \\ \widetilde{v} = v. \end{cases} \tag{41}$$

556 Therefore, the Boltzmann equation (40) can also be solved by the method presented in

557 this article in principle. However, such four-dimensional simulations are beyond the cur-

558 rent scope of the UBER code since it is only coded for up to three dimensions in space.

559 Nonlinear evolution of phase space density occurs when the particle scatterings are

560 not only small-scale but also large-scale, usually as a result of trapping by intense plasma

waves (e.g., Bortnik et al., 2008; Albert et al., 2013). In this case, the right-hand side of the kinetic equation must include terms of non-local transport of phase space density by these large-scale scatterings, and the equation is formulated as (Artemyev et al., 2018; Zheng et al., 2019)

$$\frac{\partial f}{\partial t} = \frac{1}{G}\frac{\partial}{\partial Q^{\mu}}\left(GD^{\mu\nu}\frac{\partial f}{\partial Q^{\nu}}\right) - \frac{1}{G}\frac{\partial}{\partial Q^{\mu}}\left(Gh^{\mu}f\right) - \left(\int P_{Q\to\widetilde{Q}}\,\widetilde{G}d\widetilde{Q}^{\mu}\right)f + \int P_{\widetilde{Q}\to Q}\,\widetilde{f}\widetilde{G}d\widetilde{Q}^{\mu},$$
(42)

in which $\widetilde{f}$ is a shorthand for the function $f(t,\widetilde{Q}^{\mu})$, and $\widetilde{G}$ is the Jacobian determinant evaluated at $\widetilde{Q}^{\mu}$. With nonlinear wave-particle interactions, phase bunching effect gives rise to the advection characterized by the coefficients h^{μ}. The function $P_{Q\to\widetilde{Q}}$ is the trapping probability density from Q^{μ} to $\widetilde{Q}^{\mu}$, that is, particles are trapped by the wave field at Q^{μ} and subsequently escape from trapping at $\widetilde{Q}^{\mu}$, and is considered a known function which can be evaluated from single particle behaviors by either perturbation theory of Hamiltonian mechanics (e.g., Artemyev et al., 2016) or test-particle simulations (e.g., Vainchtein et al., 2018). Note that, since the unknown function is contained in the last integral term, Eq. (42) is an integro-differential equation. However, formal similarity between Eq. (42) and the Fokker-Planck equation (1) suggests that an asymptotic solution of Eq. (42) may be achieved by Taylor expanding $\widetilde{f}$ as

$$\widetilde{f} = \widetilde{f}_0 + \widetilde{f}_0' t + \dots,$$
(43)

where $\widetilde{f}_0 = f(0,\widetilde{Q}^{\mu})$ and $\widetilde{f}_0'$ indicates its time-derivative function evaluated at $t = 0$. When applying the SDE method with a solution grid, the functions $\widetilde{f}_0$ and $\widetilde{f}_0'$ can be obtained from solutions of previous time stamps. Then, by defining the following coefficients

$$S(Q^{\mu}) = -\int P_{Q\to\widetilde{Q}}\,\widetilde{G}d\widetilde{Q}^{\mu},$$
(44)

$$v(t,Q^{\mu}) = \int P_{\widetilde{Q}\to Q}\,\widetilde{f}_0\widetilde{G}d\widetilde{Q}^{\mu} + t\int P_{\widetilde{Q}\to Q}\,\widetilde{f}_0'\widetilde{G}d\widetilde{Q}^{\mu} + \dots,$$
(45)

which are now known functions, Eq. (42) is transformed into the form of Eq. (1), and is readily solvable by the UBER code. In this way, the simulations of nonlinear wave-particle interactions in the radiation belts could hence be unified with the well-developed simulations in the quasi-linear theory.

References

Albert, J. M., Meredith, N. P., & Horne, R. B. (2009). Three-dimensional diffusion simulation of outer radiation belt electrons during the 9 October 1990 magnetic storm. J. Geophys. Res. Space Physics, 114(A9).

Albert, J. M., Tao, X., & Bortnik, J. (2013). Aspects of nonlinear wave-particle interactions. In Dynamics of the earth's radiation belts and inner magnetosphere (pp. 255–264). American Geophysical Union. doi: 10.1029/2012GM001324

Ames, W. F. (2014). Numerical methods for partial differential equations. Academic press.

Artemyev, A., Neishtadt, A., Vainchtein, D., Vasiliev, A., Vasko, I., & Zelenyi, L. (2018). Trapping (capture) into resonance and scattering on resonance: Summary of results for space plasma systems. Commun. Nonlinear Sci. Numer. Simulat.. doi: 10.1016/j.cnsns.2018.05.004

Artemyev, A., Neishtadt, A. A., A. I. and. Vasiliev, & Mourenas, D. (2016). Kinetic equation for nonlinear resonant wave-particle interaction. Physics of Plasmas, 23(9), 090701. doi: 10.1063/1.4962526

Aseev, N. A., Shprits, Y. Y., Drozdov, A. Y., & Kellerman, A. C. (2016). Numerical applications of the advective-diffusive codes for the inner magnetosphere. Space Weather, 14(11), 993-1010. doi: 10.1002/2016SW001484

Beutier, T., Boscher, D., & France, M. (1995). Salammbô: A three-dimensional simulation of the proton radiation belt. J. Geophys. Res., 100, 17181-17188.

Bolton, S. J., Janssen, M., Thorne, R., Levin, S., Klein, M., Gulkis, S., ... others (2002). Ultra-relativistic electrons in Jupiter's radiation belts. Nature, 415(6875), 987–991.

Bolton, S. J., Thorne, R. M., Bourdarie, S., de Pater, I., & Mauk, B. (2004). Jupiter's inner radiation belts. Jupiter: The Planet, Satellites, and Magnetosphere, 671.

Bortnik, J., Thorne, R. M., & Inan, U. S. (2008). Nonlinear interaction of energetic

electrons with large amplitude chorus. Geophys. Res. Lett., 35(21). doi: 10 .1029/2008GL035500

Cunningham, G. S., Loridan, V., Ripoll, J.-F., & Schulz, M. (2018). Neoclassical diffusion of radiation-belt electrons across very low L-shells. J. Geophys. Res. Space Physics, 123(4), 2884-2901. doi: 10.1002/ 2017JA024931

Dendy, R. O. (1990). Plasma dynamics. Clarendon Press, Oxford.

Elkington, S. R., Chan, A. A., Jaynes, A. N., Malaspina, D., & Albert, J. (2019). K2: Towards a comprehensive simulation framework of the Van Allen radiation belts. AGU Fall Meeting, 2019, SM44B–01.

Finlay, C. C., Maus, S., & et al. (2010). International geomagnetic reference field: the eleventh generation. Geophys. J. Int., 183(3), 1216-1230. doi: 10.1111/j .1365-246X.2010.04804.x

Fok, M.-C., Buzulukova, N. Y., Chen, S.-H., Glocer, A., Nagai, T., Valek, P., & Perez, J. D. (2014). The Comprehensive Inner Magnetosphere-Ionosphere Model. J. Geophys. Res. Space Physics, 119(9), 7522-7540. doi: 10.1002/ 2014JA020239

Freidlin, M. (1985). Functional integration and partial differential equations (No. 109). Princeton, New Jersey: Princeton Univ. Press.

Gobet, E. (2001). Euler schemes and half-space approximation for the simulation of diffusion in a domain. ESAIM: Probability and Statistics, 5, 261–297. doi: 10 .1051/ps:2001112

Goldstein, H. (1980). Classical mechanics (2nd ed.). Addison-Wesley, Reading, Mass.

Horne, R. B., Thorne, R. M., Glauert, S. A., Menietti, J. D., Shprits, Y. Y., & Gurnett, D. A. (2008). Gyro-resonant electron acceleration at Jupiter. Nature Physics, 4(4), 301–304.

Kac, M. (1949). On distributions of certain Wiener functionals. Transactions of the American Mathematical Society, 65(1), 1–13.

Klebaner, F. C. (2005). Introduction to stochastic calculus with applications. World Scientific Publishing Company.

Kloeden, P. E., & Platen, E. (1992). Numerical solution of stochastic differential equations (Vol. 23). Berlin: Springer-Verlag.

Lenchek, A. M., Singer, S. F., & Wentworth, R. C. (1961). Geomagnetically trapped electrons from cosmic ray albedo neutrons. J. Geophys. Res., 66(12), 4027-4046. doi: 10.1029/JZ066i012p04027

Lépingle, D. (1995). Euler scheme for reflected stochastic differential equations. Mathematics and Computers in Simulation, 38(1-3), 119–126.

Li, W., & Hudson, M. K. (2019). Earth's Van Allen radiation belts: From discovery to the Van Allen Probes era. J. Geophys. Res. Space Physics, 124(11), 8319-8351. doi: 10.1029/2018JA025940

Li, X., Selesnick, R., Schiller, Q., Zhang, K., Zhao, H., & Baker, M. A., Daniel N. and Temerin. (2017). Measurement of electrons from albedo neutron decay and neutron density in near-Earth space. Nature, 552(7685), 382-385. doi: 10.1038/nature24642

Lorenzato, L., Sicard, A., & Bourdarie, S. (2012). A physical model for electron radiation belts of Saturn. J. Geophys. Res. Space Physics, 117(A8). doi: 10 .1029/2012JA017560

Mathews, J., & Walker, R. L. (1970). Mathematical methods of physics (second ed.). Addison-Wesley.

Nénon, Q., Sicard, A., & Bourdarie, S. (2017). A new physical model of the electron radiation belts of Jupiter inside Europa's orbit. J. Geophys. Res. Space Physics, 122(5), 5148-5167. doi: 10.1002/2017JA023893

Øksendal, B. (1998). Stochastic differential equations (fifth ed.). Berlin: Springer.

Press, W. H., Teukolsky, S. A., Vetterling, W. T., & Flannery, B. P. (1992). Numerical recipes in FORTRAN: The art of scientific computing. Cambridge Univ. Press, New York.

Rodger, C. J., Clilverd, M. A., & McCormick, R. J. (2003). Significance of lightning-generated whistlers to inner radiation belt electron lifetimes. J. Geophys. Res. Space Physics, 108(A12). doi: 10.1029/2003JA009906

Sauvaud, J.-A., Maggiolo, R., Jacquey, C., Parrot, M., Berthelier, J.-J., Gamble, R. J., & Rodger, C. J. (2008). Radiation belt electron precipitation due to VLF transmitters: Satellite observations. Geophys. Res. Lett., 35(9). doi: 10.1029/2008GL033194

Schulz, M. (1991). The Magnetosphere. In Geomagnetism, volume 4 (pp. 87–293). Editor J. A. Jacobs. Academic Press.

686   Selesnick, R. S.   (2012).   Atmospheric scattering and decay of inner radiation

687   belt electrons.   J. Geophys. Res. Space Physics, 117(A8).   doi: 10.1029/

688   2012JA017793

689   Selesnick, R. S.   (2015).   High-energy radiation belt electrons from CRAND.

690   J. Geophys. Res. Space Physics, 120(4), 2912-2917.   doi: 10.1002/

691   2014JA020963

692   Selesnick, R. S., Blake, J. B., & Mewaldt, R. A.   (2003).   Atmospheric losses of radi-

693   ation belt electrons.   J. Geophys. Res. Space Physics, 108(A12).   doi: 10.1029/

694   2003JA010160

695   Selesnick, R. S., Hudson, M. K., & Kress, B. T.   (2013).   Direct observation of

696   the CRAND proton radiation belt source.   J. Geophys. Res. Space Physics,

697   118(12), 7532-7537. doi: 10.1002/2013JA019338

698   Serber, R.   (1992).   The Los Alamos primer: The first lectures on how to build an

699   atomic bomb. Univ of California Press.

700   Shprits, Y. Y., Chen, L., & Thorne, R. M.   (2009).   Simulations of pitch angle

701   scattering of relativistic electrons with MLT-dependent diffusion coefficients.

702   J. Geophys. Res. Space Physics, 114(A3). doi: 10.1029/2008JA013695

703   Subbotin, D., Shprits, Y., & Ni, B.   (2010).   Three-dimensional VERB radiation

704   belt simulations including mixed diffusion.   J. Geophys. Res. Space Physics,

705   115(A3). doi: 10.1029/2009JA015070

706   Tao, X., Albert, J. M., & Chan, A. A.   (2009).   Numerical modeling of

707   multidimensional diffusion in the radiation belts using layer methods.

708   J. Geophys. Res. Space Physics, 114, A02215. doi: 10.1029/2008JA013826

709   Tao, X., Chan, A. A., Albert, J. M., & Miller, J. A.   (2008).   Stochastic modeling

710   of multidimensional diffusion in the radiation belts.   J. Geophys. Res. Space

711   Physics, 113, A07212. doi: 10.1029/2007JA012985

712   Tu, W., Cunningham, G. S., Chen, Y., Henderson, M. G., Camporeale, E.,

713   & Reeves, G. D.   (2013).   Modeling radiation belt electron dynamics

714   during GEM challenge intervals with the DREAM3D diffusion model.

715   J. Geophys. Res. Space Physics, 118. doi: 10.1002/jgra.50560

716   Tu, W., Selesnick, R., Li, X., & Looper, M.   (2010).   Quantification of the

717   precipitation loss of radiation belt electrons observed by SAMPEX.

718   J. Geophys. Res. Space Physics, 115(A7). doi: 10.1029/2009JA014949

719 Vainchtein, D., Zhang, X.-J., Artemyev, A. V., Mourenas, D., Angelopoulos, V., &
720   Thorne, R. M.   (2018).   Evolution of electron distribution driven by nonlinear
721   resonances with intense field-aligned chorus waves.   J. Geophys. Res. Space
722   Physics, 123(10), 8149-8169. doi: 10.1029/2018JA025654

723 Wang, C., Ma, Q., Tao, X., Zhang, Y., Teng, S., Albert, J. M., ... Wang, S.
724   (2017).   Modeling radiation belt dynamics using a 3-D layer method
725   code.   J. Geophys. Res. Space Physics, 122(8), 8642-8658.   doi: 10.1002/
726   2017JA024143

727 Xiang, Z., Li, X., Selesnick, R., Temerin, M. A., Ni, B., Zhao, H., ... Khoo, L. Y.
728   (2019).   Modeling the quasi-trapped electron fluxes from cosmic ray albedo
729   neutron decay (CRAND).   Geophys. Res. Lett., 46(4), 1919-1928.   doi:
730   10.1029/2018GL081730

731 Xiang, Z., Li, X., Temerin, M. A., Ni, B., Zhao, H., Zhang, K., & Khoo, L. Y.
732   (2020).   On energetic electron dynamics during geomagnetic quiet times in
733   Earth's inner radiation belt due to atmospheric collisional loss and CRAND as
734   a source. J. Geophys. Res. Space Physics, 125(2). doi: 10.1029/2019JA027678

735 Zheng, L.   (2015).   Development and application of stochastic methods for radiation
736   belt simulations (Unpublished doctoral dissertation). Rice University, Houston,
737   TX.

738 Zheng, L., Chan, A. A., Albert, J. M., Elkington, S. R., Koller, J., Horne, R. B.,
739   ... Meredith, N. P.   (2014).   Three-dimensional stochastic modeling of radia-
740   tion belts in adiabatic invariant coordinates.   J. Geophys. Res. Space Physics,
741   119(9), 7615–7635. doi: 10.1002/2014JA020127

742 Zheng, L., Chan, A. A., O'Brien, T. P., Tu, W., Cunningham, G. S., Albert, J. M.,
743   & Elkington, S. R.   (2016).   Effects of magnetic drift shell splitting on elec-
744   tron diffusion in the radiation belts.   J. Geophys. Res. Space Physics, 121(12),
745   11,985–12,000. doi: 10.1002/2016JA023438

746 Zheng, L., Chen, L., & Zhu, H.   (2019).   Modeling energetic electron non-
747   linear wave-particle interactions with electromagnetic ion cyclotron
748   waves.   J. Geophys. Res. Space Physics, 124(5), 3436-3453.   doi: 10.1029/
749   2018JA026156